High resolution astronomical image restoration system for large ground-based telescope

Shixue Zhang (张世学)*, Jinyu Zhao (赵金宇), and Jianli Wang (王建立)

Changchun Institute of Optics, Fine Mechanics and Physics, Chinese Academy of Sciences, Changchun 130033, China

**Corresponding author: zhangsx@ciomp.ac.cn*

Received April 25, 2012; accepted July 4, 2012; posted online November 23, 2012

The resolution of astronomical imaging from large optical telescopes is usually limited by the blurring effects of refractive index fluctuations in the Earth's atmosphere. In this letter, we develop a lucky imaging system to restore astronomical images through atmosphere turbulence on large telescope. Our system takes very short exposures, on the order of the atmospheric coherence time. The rapidly changing turbulence leads to a very variable point spread function (PSF), and the variability of the PSF leads to some frames having better quality than the rest. Only the best frames are selected, aligned and co-added to give a final image with much improved angular resolution. Our lucky imaging system is successfully applied to restore the astronomical images taken by a 1.23 m telescope. We get clear images of moon surface, Jupiter, and Saturn, and our system can be demonstrated to greatly improve the imaging resolution through atmospheric turbulence.

OCIS codes: 100.3020, 010.1290, 010.7060.
doi: 10.3788/COL201210.S21004.

The resolution of all large ground-based telescopes is severely limited by the effects of atmospheric turbulence. At even the best sites, the resolution of large telescope is degraded by at least a factor of five in the visible. The recovery of the full theoretical resolution of large telescopes in the presence of atmospheric turbulence has been a major goal of technological developments in the field of astronomical instrumentation in the past decades[1−6].

Lucky imaging technique offers a particularly elegant and uncomplicated solution to the blurring effects of atmospheric turbulence. The short-exposure frames recorded by lucky imaging system are sorted according to quality; only the best frames are aligned and co-added to produce a final image. The details of the lucky imaging process, such as the frame selection and image calibration, can all be optimized during post-processing of the data. Lucky imaging is a passive technique, so useful data is taken as soon as the telescope is pointed correctly without any other special requirement.

Lucky imaging technique is being successfully employed since the 1990s using video-cameras[7] and even by amateur astronomers with small webcams. Notice that, among other advantages, lucky imaging is cheaper than adaptive optics and with a lower dependence on the presence of reference stars.

All high-resolution imaging systems are limited in the size of telescope for which they can adequately correct the turbulence-induced wavefront errors-there is simply more turbulence to correct as the area of the telescope increases.

As the telescope area increases, the probability of getting a diffraction-limited short-exposure image decreases rapidly. Fried[8] coined the term "lucky exposures" to describe such frames (defined as the phase errors across the telescope aperture having a root mean square (RMS) error of <1 rad). He found that the probability P of getting a diffraction-limited image varies as

$$P \approx 5.6 \exp[-0.1557(D/r_0)^2], \quad (1)$$

where D is the telescope diameter. The expression assumes a telescope that has several turbulence cells across its diameter ($D/r_0 > 4$), and that the only variations in the turbulence follow Kolmogorov statistics[9]. Under these assumptions, given a value of r_0, the probability of getting a good image is quite high on relatively small telescopes and very low on larger telescopes (essentially zero for a 10-m telescope).

Lucky imaging benefits from using large telescope apertures in two ways. Firstly, more light is collected by the telescope, allowing fainter guide stars and thus imaging over a larger area of the sky, as well as imaging of fainter science targets. Secondly, larger telescope apertures have smaller diffraction limits, increasing the final resolution of the system. It is thus beneficial to use as large a telescope as can be managed while still having a reasonable probability of obtaining diffraction-limited frames.

A number of instruments have been specifically designed to take advantage of rapidly varying seeing statistics. Most of these instruments use integration times in the range of seconds (to reduce readout noise), and thus could not perform true lucky imaging, or reach anywhere near diffraction-limited performance. They provide, however, useful improvements in the apparent seeing. There are two main classes of this type of instrument: cameras with optics or electronics designed to recenter and select images during integration, and direct short exposure imagers where the final image reconstruction is undertaken offline.

The choice of the installation location must comply with the requirements of the oil field. It must not be a place close to the storage compartments of dangerous goods. The electricity power supply system must be installed within a compartment which is able to sustain explosion.

HRCam[10] is an example of the first class of instrument. Used on the Canada-France-Hawaii telescope

(CFHT), it incorporated a fast tip/tilt mirror to follow centroid image motion and a shutter to reject periods of poorer seeing. It typically achieved 10-20% improvements in full-width at half-maximum (FWHM) resolution[11].

An instructive example of the second, offline data-processing class of instruments is described in Ref. [12]. Using the European Space Agency Photon-Counting Detector[13] with effective integration times of 1.5–20 seconds, they selected and recentered images to form final science images with FWHM resolutions improved by 30 percent[14]. Nieto *et al.*[15] described some more details of the reconstruction process. Crucially, because their integrations times were so long, their images did not have a speckled character. The system thus does not retain diffraction-limited imaging, but rather takes advantage of long-timescale changes in the seeing itself. They also aligned images on the basis of the image centroid, which removed the tip/tilt component of the turbulence but did not allow diffraction-limited image reconstruction even if the imaging frame rate was high. The benefits of alignment on the brightest speckle rather than the image centroid were discussed in detail in Ref. [16].

More recently, fast charge-coupled device (CCD) imagers have enabled near diffraction-limited lucky imaging on both relatively small telescopes of 0.36 m[17], and medium-sized telescopes (60 inch)[18]. The availability of cheap webcams has also allowed amateur astronomers to perform automated frame selection and alignment imaging. However, the high noise introduced by running these CCD-based systems fast enough to sample the atmospheric coherence time requires very bright (generally planetary) targets.

The Cambridge Lucky Imaging system (LuckyCam) is based on an E2V Technologies L3CCD read out with a 4-MHz pixel rate and mounted at the focus of a simple reimaging camera. The on-chip gain stage of the L3CCD raises the signal from incoming light sufficiently to allow individual photons to be detected with good signal to noise, even at high frame rates[19−22].

In our algorithm, the preprocessing includes dark frame subtraction, flat fielding, and cosmic ray spike elimination. Normally we take a serial of short exposure frames with the guide window closed, and average them to get the reference picture. Then this reference picture is subtracted from each of the raw frame. For the flat fielding, the similar operation is performed except that we take the pictures at dusk with the guide window open. Most of the time, we also need to remove hot pixels and readout signal which creates the vertical stripes. We use the method in Ref. [23] to eliminate these effects.

The standard lucky imaging technique selects frames on the basis of the degree of correlation to a diffraction-limited point spread function (PSF).

For point object, or there is guide star in the image, our system uses Strehl ratio (the ratio of the peak flux to that expected in a diffraction-limited core) based metric to evaluate the image quality. This procedure selects the frames with the best light concentration–that is, the frames with the largest fraction of the flux within the diffraction-limited core. It thus produces images with a maximized output on-axis Strehl ratio.

For the extended object with no guide star in our seeing, our system can use Fisher information or Sobel operator based metric to evaluate the quality.

The Fisher information of an image is calculated as

$$F = \sum_{x,y} \frac{|\nabla\psi(x,y)|^2}{\psi(x,y)} = 4\sum_{x,y}\left|\nabla\sqrt{\psi(x,y)}\right|^2,$$
$$\psi(x,y) = \frac{I_i(x,y)}{\sum\limits_{x,y} I_i(x,y)}, \tag{2}$$

where $I(x,y)$ is the image value, ∇ is the gradient operator. If an image has a greater F value, then this image is clearer; on the contrary, an image with smaller F value may be more blurred. So we can use F value to evaluate the image quality, and sort the original frame sequence.

We also derive a Sobel operator based method to evaluate the image quality. Sobel operator is widely used in edge detection. Traditional Sobel operator applies the convolution operation to the image with two 3×3 template matrix. The two templates are

$$S_x = \begin{pmatrix} -1 & 0 & 1 \\ -2 & 0 & 2 \\ -1 & 0 & 1 \end{pmatrix}, \quad S_y = \begin{pmatrix} -1 & -2 & -1 \\ 0 & 0 & 0 \\ 1 & 2 & 1 \end{pmatrix}, \tag{3}$$

where S_x is the horizontal template, and S_y is the vertical template. Thus the Sobel operator can be represented by

$$H = \sqrt{H_x^2 + H_y^2} = \sqrt{(I(x,y) * S_x)^2 + (I(x,y) * S_y)^2}, \tag{4}$$

where $*$ is the convolution operator.

Traditional Sobel operator has templates of two directions, while our algorithm extended this to eight directions. This improved algorithm can detect edges along more directions, so it can solve the direction limitation of the traditional method. We use the sum of edge gradient to evaluate the image quality as

$$E = \sum_{x=1}^{M}\sum_{y=1}^{N} |F(x,y)|^2. \tag{5}$$

If an image is well focused, it must contain more details, so the E value of the image may be greater; on the contrary, an image with smaller E value may be more degraded.

We have validated both of the two image evaluation functions on our 1.23-m telescope. The extended Soble based metric is more accurate than Fisher information metric, although it is more time consuming.

Image registration is an important part in our algorithm, and the registration precision directly affects the quality of the final image. We also treat point object differently with extended object.

For point object, we simply use brightest point or centroid matching.

For extended object, when the background noise is not prominent, we prefer to use Fourier-Mellin transform[24,25] to make an accurate registration. Fourier-Mellin transform is a Fast fourier transform (FFT) based technique for translation, rotation, and scale-invariant image registration. We have implemented a GPU based Fourier-Mellin registration in our system,

and it can greatly reduce the processing time. For most of the time, this method can register object with complicated texture precisely.

If the images contain strong background noise, the Fourier-Mellin transform may be invalid. To make a robust registration, we prefer to use scale invariant feature transform (SIFT) method[26,27] although it is a little time consuming.

The calibrated images need to be co-added to construct a final image. The addition continues until a user-specified selection level (such as the best 5% of frames) is reached, upon which an output image is written.

If the images were simply interpolated by the non-integer pixel shifts and added, each input pixel would be reduced in resolution. To see this, consider a frame to be shifted by 1/2 of a pixel horizontally and vertically. Each pixel of the image is then spread equally over 4 pixels of the output image–thus reducing the output resolution. However, more complicated algorithms can avoid much of this resolution loss, essentially by reducing the size of the input pixel relative to those of the output image.

Our system selects to co-add the images using a custom implementation of the Drizzle algorithm[28], which offers the resolution achieved by the sinc-resampling methods without any associated ringing.

Drizzle proceeds by "drizzling" the input pixels onto a larger grid, generally 2× the size of the input pixel grid (Fig. 1). This process can also be represented by making each input pixel decrease in size (but not separation) by a factor of two before addition. At each stage of the addition both the output image and a weight map for each pixel is updated.

Each input pixel is dropped onto an area of the output grid that usually overlaps several pixels. If the fractional area of overlap with a single output pixel is represented by F, the signal $S(x, y)$ and weights $W(x, y)$ of that pixel are updated to be

$$W(x,y) = F * W_P(x,y) + W'(x,y),$$
$$S(x,y) = \frac{F * W_P(x,y) * S_{\text{input}} + S'(x,y) * W'(x,y)}{W(x,y)}, \tag{6}$$

where S' and W' denote the current signals and weights, respectively, S_{input} is the signal from the input pixel, and $W_P(x, y)$ is individual pixel weight for the current frame that can be used to remove cosmic ray affected areas.

This operation corresponds to making a weighted average of the input pixel values in each output pixel. After each frame addition $S(x, y)$ contains an estimate of the final high-resolution image.

The above processing produces an image that averages the frames with high-quality. As a final step, we perform an image enhancement method to further increase the display contrast.

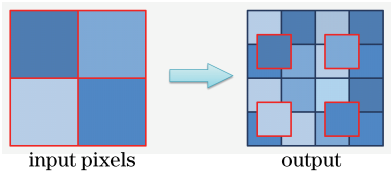

Fig. 1. Drizzle process. Input pixels are reduced in size, and drizzled onto a higher resolution output grid.

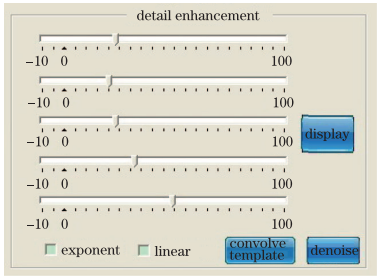

Fig. 2. User interface of image enhancement.

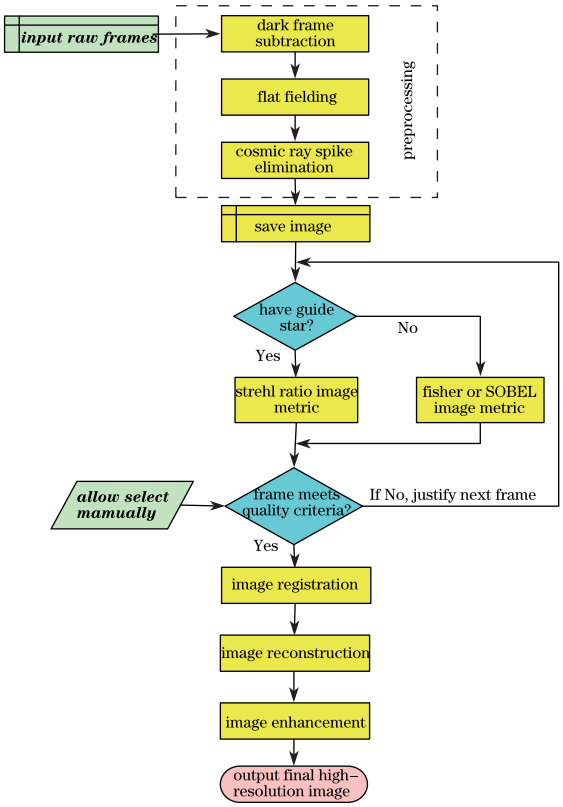

Fig. 3. Lucky imaging system pipeline.

We use five layers with predefined convolution mask to improve the final image. The user can adjust the stretch coefficient for each layer, and fine details which are degraded in the original images may appear much clearer. The user interface is shown as Fig. 2. The working pipeline of our system can be summarized as Fig. 3.

Our lucky imaging system has been successfully applied to image restoration on a 1.23-m telescope. Figure 4 shows our restoration result of the moon surface. The biggest annular mountain is BLANCANUS located at west longitude of 21.5°, south latitude of 63.6°, and its diameter is about 109 kilometer. We have continuously taken about 1 000 frames with explosion time of 10 ms, and we finally selected 20% of them to reconstruct the final image. Many fine details that are degraded in the original image can be seen clearly in our restored image. So image resolution is greatly improved by our lucky imaging system. An illustration of the Fisher information based image quality evaluation curve is shown in Fig. 5. We can see that the image quality varies randomly among the whole frames, and that basically corresponds with the atmosphere turbulence. Figure 6 shows the restoration

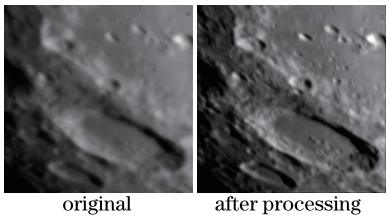

Fig. 4. Restoration of moon surface.

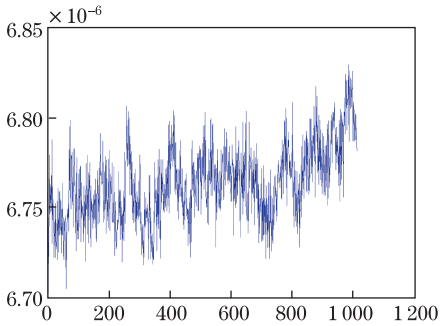

Fig. 5. Image quality metric by Fisher information.

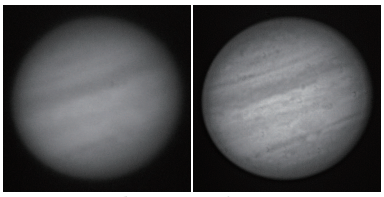

Fig. 6. Restoration of Jupiter.

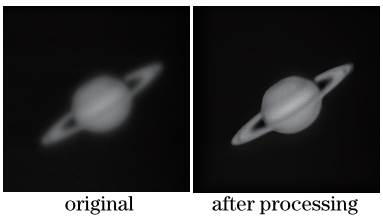

Fig. 7. Restoration of Saturn.

result of the Mars image. The output image shows a visibly much improved resolution. Especially the fine textures of Mars can be seen much clearly in the restored image. Figure 7 shows the restoration result of the Saturn image. The reconstructed image is much clear than the raw image. Thus we can demonstrate that our lucky imaging system can greatly improve the imaging resolution through atmosphere turbulence.

In conclusion, we design a lucky imaging system to restore astronomical images taken by a 1.23-m telescope. The frames recorded by our lucky imaging system are sorted according to quality; only the best frames are aligned and co-added to produce a final image with much improved angular resolution. The experimental results show that our system can greatly improve the imaging resolution and generate much improved astronomical images through atmosphere turbulence.

The authors would like to thank Electro-Optical Detection Department, Changchun Institute of Optics, Fine Mechanics and Physics, Chinese Academy of Sciences, for providing raw astronomical images. The work was supported by the National "863" Program of China under Grant No. 2008AA8080202.

References

1. M. C. Roggemann and B. Welsh, *Imaging through turbulence* (CRC press, Boca Raton, 1996).
2. B. Wang, Z. Wang, J. Wang, J. Zhao, Y. Wu, S.Zhang, L. Dong, and M. Wen, Opt. Precision Eng. (in Chinese) **19,** 1384 (2011)
3. J. Zhao, Z. Chen, B. Wang, Z. Wang, N. Zhang, J. Wang, Y. Wu, and S. Zhang, Opt. Precision Eng. (in Chinese) **20,** 431 (2012)
4. J. Wang, Z. Wang, B. Wang, Y. Wu, J. Zhao, H. Li, L. Dong, and S. Zhang, Opt. Precision Eng. (in Chinese) **19,** 1165 (2011)
5. J. Zhang, Z. Wang, and Y. Li, Opt. Precision Eng. (in Chinese) **19,** 168 (2011)
6. B. Wen, Q. Zhang, and J. Zhang, Opt. Precision Eng. (in Chinese) **19,** 3049 (2011)
7. R. F. Dantowitz, Sky and Telescope **6,** 48 (1998).
8. D. L. Fried, J. Opt. Soc. Am. **68,** 1651 (1978).
9. A. N. Kolmogorov, in *Proceedings of the Royal Society of London, Series A*: *Mathematical and Physical Sciences* **434,** 9 (1991).
10. R. D. Mcclure, W. A. Grundmann, W. N. Rambold, J. M. Fletcher, E. H. Richardson, J. R. Stillburn, R. Racine, C. A. Christian, and P. Waddell, Publications of the Astronomical Society of the Pacific **101,** 1156 (1989).
11. D. Crampton, R. D. Mcclure, and J. M. Fletcher, Astrophysical Journal **392,** 23 (1992).
12. J. L. Nieto, A. Llebaria, and S. di Serego Alighieri, Astronomy and Astrophysics **178,** 301 (1987).
13. S. di Serego Alighieri, and M. A. C. Perryman, in *Proceedings of the Meeting in Instrumentation in astronomy VI*, Part 1 (A87-36376 15-35), (1986).
14. J. L. Nieto, S. Roques, A. Llebaria, C. Vanderriest, G. Lelievre, S. di Serego Alighieri, F. D. Macchetto, and M. A. C. Perryman, Astrophysical Journal **5,** 644 (1988).
15. J. L. Nieto and E. Thouvenot, Astronomy and Astrophysics **241,** 663 (1991).
16. J. C. Christou, Publications of the Astronomical Society of the Pacific **103,** 1040 (1991).
17. J. Davis and J. R. North, Publications of the Astronomical Society of Australia **18,** 281 (2001).
18. R. F. Dantowitz, S. W. Teare, and M. J. Kozubal, Astronomical Journal **119,** 2455 (2000).
19. A. G. Basden, C. A. Haniff, and C. D. Mackay, Monthly Notices of the Royal Astronomical Society **345,** 985 (2003).
20. C. Mackay, A. Basden, and M. Bridgel, Proc. SPIE **5499,** 203 (2004).
21. N. M. Law, C. D. Mackay, and J. E. Baldwin, Astronomy and Astrophysics **446,** 739 (2006).
22. N. M. Law, The Observatory **127,** 71 (2007).
23. website: http://photo.net/learn/dark_noise/
24. Q. S. Chen, M. Defrise, and F. Deconinck, IEEE Transactions on Pattern Analysis and Machine Intelligence **16,** 1156 (1994).
25. B. R. Srijivasa and B. N. Chatterji, IEEE Transactions on Image Processing **5,** 1266 (1996).
26. D. G. Lowe, in *Proceedings of International Conference on Computer Vision* 1150 (1999).
27. D. G. Lowe, International Journal of Computer Vision **60,** 91 (2004).
28. A. S. Fruchter and R. N. Hook, Publications of the Astronomical Society of Australia **114,** 144 (2002).